Geophysical Research Letters

RESEARCH LETTER
10.1029/2023GL104077

Key Points:

- A new method of 3-D adjoint tomography for receiver function inversion is developed
- Lateral heterogeneities of crust and uppermost mantle can be well resolved by this method
- The method reveals vertically extending low-velocity zones under the Red River Fault due to mantle upwelling

Supporting Information:

Supporting Information may be found in the online version of this article.

Correspondence to:

P. Tong,
tongping@ntu.edu.sg

Citation:

Xu, M., Wang, K., Chen, J., Yu, D., & Tong, P. (2023). Receiver function adjoint tomography for three-dimensional high-resolution seismic array imaging: Methodology and applications in Southeastern Tibet. *Geophysical Research Letters*, *50*, e2023GL104077. https://doi.org/10.1029/2023GL104077

Received 14 APR 2023
Accepted 11 SEP 2023

Author Contributions:

Conceptualization: Mijian Xu, Kai Wang
Data curation: Dayong Yu
Formal analysis: Mijian Xu, Jing Chen
Funding acquisition: Dayong Yu, Ping Tong
Investigation: Mijian Xu, Jing Chen
Methodology: Mijian Xu, Kai Wang, Ping Tong
Project Administration: Ping Tong
Resources: Dayong Yu, Ping Tong
Software: Mijian Xu, Kai Wang
Supervision: Ping Tong
Validation: Mijian Xu, Jing Chen
Visualization: Mijian Xu

Receiver Function Adjoint Tomography for Three-Dimensional High-Resolution Seismic Array Imaging: Methodology and Applications in Southeastern Tibet

Mijian Xu[1,2], Kai Wang[2,3], Jing Chen[1], Dayong Yu[4], and Ping Tong[1,2,5]

[1]Division of Mathematical Sciences, School of Physical and Mathematical Sciences, Nanyang Technological University, Singapore, Singapore, [2]Earth Observatory of Singapore, Nanyang Technological University, Singapore, Singapore, [3]School of Earth and Space Sciences, University of Science and Technology of China, Hefei, China, [4]School of Earth Sciences and Engineering, Nanjing University, Nanjing, China, [5]Asian School of the Environment, Nanyang Technological University, Singapore, Singapore

Abstract A new technique for P-wave receiver function (PRF) inversion, within the framework of wave equation-based adjoint tomography and referred to as receiver function adjoint tomography (RFAT), has been developed to obtain models of *Vp*, *Vs*, and density. This innovative technique fits the synthetic PRFs with observed PRFs and can better image the lateral variations of *Vs* from the crust to the uppermost mantle than traditional 1-D PRF inversion. We utilized RFAT to perform high-resolution imaging beneath a dense seismic array in Southeastern Tibet, revealing low-velocity zones extending from the uppermost mantle to the crust, as well as an eastward dipping Moho under the Red River Fault (RRF). Our inversion results provide direct evidence for the existence of a distinct asthenospheric upwelling channel beneath the RRF, and further highlight the effectiveness of RFAT for accurately imaging subsurface structures.

Plain Language Summary We have developed a novel technique that allows for direct inversion of P-wave receiver functions for a detailed 3-D S-wave velocity model. By applying this technique to a dense seismic array located in the southeastern margin of the Tibetan Plateau, we can resolve detailed crustal and uppermost mantle structures with strong lateral variations. The results indicate that the boundary faults of the geological blocks play a critical role in controlling the lateral variations of the crustal and upper mantle structures. Our findings provide new insights into the dynamics of lithosphere-asthenosphere interactions and continental collision processes in this region.

1. Introduction

The P-wave receiver function (PRF) is extracted from the P wave coda by deconvoluting the vertical component of a teleseismic waveform from its radial component (Langston, 1979; Ligorría & Ammon, 1999). Traditional PRF imaging techniques, including common conversion point (CCP) stacking (Dueker & Sheehan, 1997), $H-\kappa$ stacking (L. Zhu & Kanamori, 2000), and 1-D inversion of PRFs (either alone or in combination with surface wave dispersions (SWDs)) (Ammon et al., 1990; Bodin et al., 2012; Julià et al., 2000), use scattered phases embedded in PRFs such as Ps and PpPs to determine subsurface discontinuity depths and S-wave velocity structures. It is crucial to note that phases in PRFs are generated not only by subsurface discontinuities but also by potential irregular scatterers. However, the above-mentioned methods assume that the subsurface has a 1-D horizontal layered subsurface structure, which limits their ability to image 3-D subsurface structure with strong lateral heterogeneities (e.g., subduction zones and continental orogenic belts), where P-wave coda may be generated by complex scatterers instead of horizontal discontinuities.

To overcome the limitations of traditional PRF techniques, it is important to consider the influence of finite frequency effects of teleseismic P-wave coda on the interaction between wave propagation and complex heterogeneities (Monteiller et al., 2015; Tong et al., 2014a). In a recent study, de Jong et al. (2022) has calculated 2-D finite frequency misfit kernels of PRFs based on the wave equation and the adjoint method (Q. Liu & Tromp, 2008; Tromp et al., 2005), which allows for the integration of PRFs-based objective functions and the adjoint tomography workflow. Compared to ray-based imaging methods of PRFs (e.g., weighted CCP stacking (Lekic et al., 2011) and Kirchhoff migration (Hansen & Schmandt, 2017)), finite frequency kernels provide a wider sensitivity region and simultaneously consider the effects of single and multiple scattered phases (de Jong

Writing – original draft: Mijian Xu
Writing – review & editing: Kai Wang, Jing Chen, Dayong Yu, Ping Tong

et al., 2022). These kernels, sensitive to velocities and density, provide an accurate account of complex wave propagation effects in heterogeneous media. Therefore, finite-frequency based inversion of PRFs can provide better resolving ability in laterally heterogeneous structures than 1-D inversion based on a layered model.

Teleseismic full-waveform inversion (FWI) also uses finite-frequency misfit kernels to invert for velocity and density models with a nonlinear iterative algorithm (Monteiller et al., 2015; K. Wang et al., 2021a). This method has been applied to continental subduction zones to constrain lateral heterogeneities (Beller et al., 2018; K. Wang et al., 2021b; Y. Wang et al., 2016). However, teleseismic FWI needs high-quality coherent P coda waves on vertical and radial components, which are rare in real data due to complex source spectral contents (Beller et al., 2018), especially for high frequency data. Thus, previous studies only selected ∼10 teleseismic events and used a maximum frequency of ∼0.2 Hz, resulting in limited model resolution. In contrast, PRFs remove source signature by deconvolution and analyze high frequency data with a higher maximum frequency. Furthermore, it is possible to stack PRFs with similar back-azimuths and ray-parameters to improve the signal-to-noise ratio of the data. Thus, the inversion of PRFs utilizing a finite-frequency approach has a potential to generate higher-resolution subsurface images than the teleseismic FWI.

This study develops an inversion scheme called receiver function adjoint tomography (RFAT) for dense seismic array imaging. Within the framework of 3-D adjoint tomography, we utilize the spectral-element and frequency-wavenumber (SEM-FK) methods (Tong et al., 2014a, 2014b) to simulate teleseismic waveforms in a 3-D local domain and compute misfit kernels of the PRFs with the adjoint method. We apply this new method to perform dense seismic array imaging in Southeastern Tibet, revealing the lateral heterogeneities of velocity structures in the crust and uppermost mantle, which are not imaged by previous traditional inversion of PRFs.

2. Methodology

2.1. Adjoint Method for PRFs

In the process of PRF inversion, the objective function χ is defined as the waveform misfit between N sets of synthetic PRFs (RF^{syn}) generated by modeling the data in a parameterized velocity and density model $\mathbf{m}$, and the observed PRFs (RF^{obs}), written as

$$\chi = \frac{1}{2}\sum_{i=1}^{N}\int_{0}^{T} W(t)w_i\left[\mathrm{RF}_i^{\mathrm{syn}}(\boldsymbol{x}_r,\boldsymbol{m},t) - \mathrm{RF}_i^{\mathrm{obs}}(\boldsymbol{x}_r,t)\right]^2 \mathrm{dt} \tag{1}$$

where $\boldsymbol{x}_r$ represents the position of the receiver, $W(t)$ is the time window function, w_i is the weight of the ith set of data. The perturbation of the misfit $\delta\chi$ can be expressed by:

$$\delta\chi = \int (K_\rho \delta \ln\rho + K_\alpha \delta \ln\alpha + K_\beta \delta \ln\beta) d^3\boldsymbol{x} \tag{2}$$

where K_ρ, K_α, and K_β are sensitivity kernels with respect to model parameters of density (ρ), Vp (α), and Vs (β) (Q. Liu & Tromp, 2006; Tromp et al., 2005). These sensitivity kernels are used to update the model parameters using an optimization algorithm, such as the Limited-memory Broyden–Fletcher–Goldfarb–Shanno (L-BFGS) method (D. C. Liu & Nocedal, 1989). The sensitivity kernels can be computed via the adjoint method, which involves the interaction between the forward and adjoint wavefields. To obtain the adjoint wavefield, an adjoint simulation is performed by putting time-reversed adjoint sources at receiver positions (Tromp et al., 2005). In general, an adjoint source is defined as the derivative of the misfit function with respect to the synthetic waveform (Fichtner et al., 2006; Tromp et al., 2005). For the inversion of PRFs, the adjoint sources in the frequency domain $F^\dagger = \left(F_R^\dagger, F_Z^\dagger\right)$ can be derived based on Parseval's theorem (de Jong et al., 2022)

$$F_R^\dagger(\boldsymbol{x},\omega) = \frac{\Delta\widehat{RF}(\boldsymbol{x}_r,\boldsymbol{m},\omega)}{\hat{\boldsymbol{u}}_Z^*(\boldsymbol{x}_r,\boldsymbol{m},\omega)}\delta(\boldsymbol{x}-\boldsymbol{x}_r)$$

$$F_Z^\dagger(\boldsymbol{x},\omega) = -\frac{\Delta\widehat{RF}(\boldsymbol{x}_r,\boldsymbol{m},\omega)\hat{\boldsymbol{u}}_R^*(\boldsymbol{x}_r,\boldsymbol{m},\omega)}{\hat{\boldsymbol{u}}_Z^{2*}(\boldsymbol{x}_r,\boldsymbol{m},\omega)}\delta(\boldsymbol{x}-\boldsymbol{x}_r) \tag{3}$$

where $\Delta\hat{\mathrm{RF}}$ represents the difference between the synthetic and observed PRFs in the frequency domain, $\hat{\boldsymbol{u}}_R$ and $\hat{\boldsymbol{u}}_Z$ are the radial and vertical components of the synthetic displacement in the frequency domain, respectively.

The superscript * represents the conjugate operator. Alternatively, with a time window $W(t)$ applied, the adjoint sources in the time domain are given by

$$f_R^\dagger(\boldsymbol{x},t) = W(t)[\Delta RF(\boldsymbol{x}_r,\boldsymbol{m},t) \oslash \boldsymbol{u}_Z(\boldsymbol{x}_r,\boldsymbol{m},T-t)]\delta(\boldsymbol{x}-\boldsymbol{x}_r)$$

$$f_Z^\dagger(\boldsymbol{x},t) = -W(t)[\Delta RF(\boldsymbol{x}_r,\boldsymbol{m},t) \circledast \boldsymbol{u}_R(\boldsymbol{x}_r,\boldsymbol{m},T-t) \oslash (\boldsymbol{u}_Z \circledast \boldsymbol{u}_Z)(\boldsymbol{x}_r,\boldsymbol{m},T-t)]\delta(\boldsymbol{x}-\boldsymbol{x}_r) \quad (4)$$

where T represents the time length of $W(t)$, the symbols $\circledast$ and $\oslash$ represent convolution and deconvolution operators, respectively. In this study, we adopt the time-domain iterative deconvolution method (Ligorría & Ammon, 1999) to calculate the time-domain adjoint sources.

2.2. Inversion Workflow of RFAT

We adopt a general workflow of adjoint tomography for RFAT. During each iteration of the workflow: (a) Synthetic teleseismic waveforms are simulated using the SEM-FK hybrid method (Tong et al., 2014a, 2014b). (b) Synthetic PRFs are calculated using the same filtering parameters and deconvolution method as the observed PRFs. (c) Adjoint wavefields are computed by solving a time-reversal wave equation with summing adjoint sources from different frequency bands, which allows us to obtain the event sensitivity kernels. Note that an event sensitivity kernel is computed using data from one virtual event to all stations that receive data from the same source region. The event kernels are scaled by multiplying the depth to suppress large sensitivities near receivers. (d) The rescaled event kernels are summed with a geographical weighting technique to balance spatial biases arising from the uneven event distribution (Ruan et al., 2019). The summed kernels are subsequently smoothed with a Gaussian function to obtain the final misfit gradient (K. Wang et al., 2021a; H. Zhu et al., 2015). (e) The model perturbation is computed using the L-BFGS method based on the misfit gradient (D. C. Liu & Nocedal, 1989), where the optimal step length is determined using a linear search method (H. Zhu et al., 2015).

3. Application to a Seismic Array in the SE Tibet

The Ailaoshan-Red River shear zone (ARSZ) is located in the southeastern Tibet between the Yangtze Craton and the Indochina block, and is bounded by the Red River Fault (RRF) and the Ailaoshan Fault (Figure 1a). Our previous study shows distinctly different characteristics of PRFs at different back-azimuths near the RRF, indicating either single or multiple scattering due to strong lateral variations of velocities (M. Xu et al., 2022). These PRFs also cannot be accurately predicted by the 1-D joint inversion of PRFs and SWD curves (hereafter called 1-D joint inversion for brevity) (M. Xu et al., 2022). Therefore, a new 3-D tomographic technique for PRFs is essential for imaging lateral heterogeneities throughout the ARSZ, considering all potential scattering effects.

3.1. Data Processing and Model Construction

We collected waveforms of 876 teleseismic events with an epicentral distance of 30°–90° recorded by 40 stations across the ARSZ (Figures 1a and 1b). Teleseismic waveforms were filtered in a frequency band of 0.05–1.0 Hz, which surpasses the maximum frequency of ∼0.2 Hz in previous applications of teleseismic FWI (Beller et al., 2018; K. Wang et al., 2021b; Y. Wang et al., 2016). Utilizing a previous workflow (M. Xu et al., 2020), we calculated a total of 7110 PRFs with a Gaussian factor of 1.0 and 8341 PRFs with a Gaussian factor of 1.5, following a manual quality control process. The two Gaussian factors correspond to cut-off frequencies of ∼0.48 and ∼0.72 Hz, respectively. In the objective function, based on the normalization of the Gaussian filter amplitudes, PRFs in these two frequency bands are assigned equal weights. To suppress noise and reduce computation, the agglomerative clustering method (Murtagh & Legendre, 2014) was used to group the teleseismic events into 31 clusters based on their similar back-azimuths and ray-parameters (Figure 1c). Similar waveforms are classified into the same cluster (Figure S1 in Supporting Information S1). Having excluded clusters with less than 15 PRFs, we retained 25 clusters as virtual events. Subsequently, we stacked the PRFs from the same cluster for adjoint tomography (Figure 1d). The objective function is measured in a time window spanning from 5 s before to 25 s after the first P arrival. This time window encompasses potential Ps phases generated by scattering in both the crust and uppermost mantle, as well as potential multiple phases generated by scattering in the crust. We then determined the weight of each virtual event using the geographic weighting method (Ruan et al., 2019).

We adopt the SEM-FK method (Tong, et al., 2014a, 2014b) for forward simulations of synthetic P-coda wavefields. The simulation domain covers a region from 101.5°E to 105°E, from 22.4°N to 23.6°N, and from the surface to

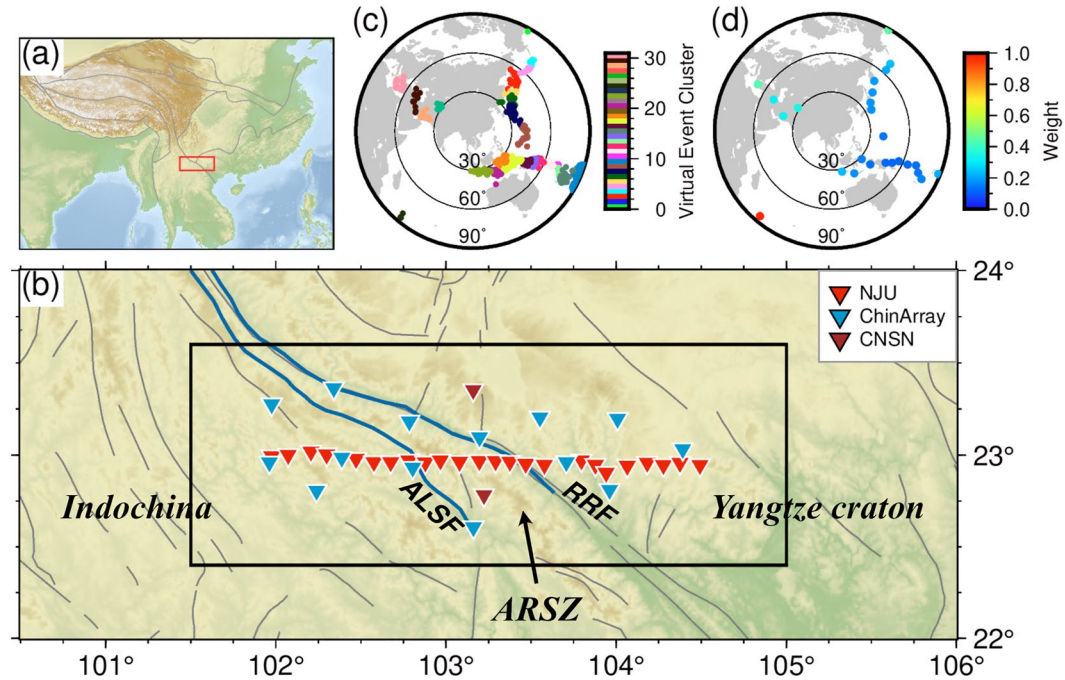

Figure 1. (a) Tectonics in the SE Asia. Gray lines denote major tectonic boundaries. The red box shows the study region. (b) Topographic map of the Ailaoshan-Red River shear zone and adjacent regions. The 24 red triangles denote seismic stations deployed by Nanjing University (NJU). The 14 blue triangles denote stations deployed by the ChinArray project. The two brown triangles are stations from China National Seismic Network. Blue lines represent boundary faults. The black box shows the boundaries of the model. The abbreviations are ALSF: Ailaoshan Fault; ARSZ: Ailaoshan Red River shear zone; RRF: Red River Fault. (c) Earthquakes with agglomerative clustering. The earthquakes are grouped into 31 clusters indicated by different colors. (d) Locations of virtual events. Colors denote weights of events.

100 km depth, incorporated with the surface topography (Figure 2a). The domain is constructed on a Cartesian grid consisting of 96 × 36 × 25 elements, giving a maximum resolving frequency of ∼0.7 Hz. This is necessary because the minimum wavelength should be approximately larger than the size of 4.5 grid points. We obtain the initial model (**M**00) from a regional 3-D velocity model created using surface wave tomography (Figure S2 in Supporting Information S1) (Z. Zhang et al., 2020b). The initial plane wavefield of P-wave is computed using the FK method with specified back-azimuths and take-off angles of each virtual event. To mitigate scattering when injecting the plane wavefield from the FK domain to the SEM domain, a buffer zone with a width of 25 km is implemented at each lateral boundary of the SEM domain, connecting a two-layer model for numerical simulation using the FK method with the initial model (Figure 2a). The Stacey absorbing boundary condition (Stacey, 1988) is applied at the boundaries of the SEM domain. Following the inversion workflow described in Section 2.2, we implemented the RFAT to obtain optimal *Vp*, *Vs* and density models (see Text S1 in Supporting Information S1 for detailed procedure and parameters).

3.2. Sensitivity Kernels

We selected a virtual event recorded by one station (the magenta triangle in Figure 2a) to demonstrate how sensitivity kernels are computed. The Pms phase is visible at ∼4.5 s in the observed PRF, while it is at ∼5.0 s in the synthetic PRF computed in the **M**00 (Figure 2b). To emphasize the sensitivity of this specific phase, we employed Equation 4 to determine the radial and vertical components of the adjoint source, which were windowed from 2.5 to 7.5 s after the P arrival (Figure 2c). Figures 2d–2i show sensitivity kernels of the PRF with respect to *Vp*, *Vs*, and density. These kernels resemble the 2-D kernels of teleseismic waveforms (Tong et al., 2014a), ray-based kernels of PRFs (Hansen & Schmandt, 2017; Millet et al., 2019), and 2-D waveform-derived kernels of PRFs (de Jong et al., 2022). Both the *Vp* and *Vs* kernels highlight the regions of influence on the Pp and PpPp phase. The *Vs* kernel also identifies the region of influence on Ps, which is the main phase recorded by the PRFs. Although the initial model has a Moho depth of ∼35 km, the sensitivity range of the Pms phase can extend to ∼50 km.

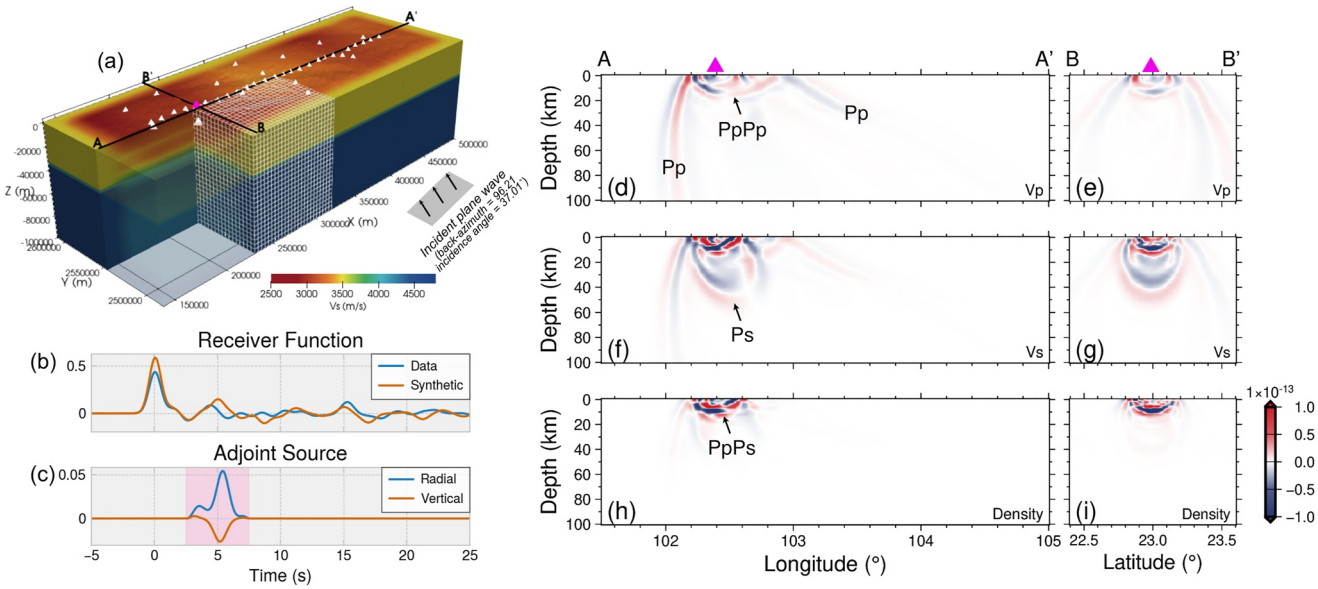

Figure 2. (a) The computational domain and initial model for the 3-D receiver function adjoint tomography of this study. The white grids denote the mesh used in this study. White triangles represent seismic stations. Black lines denote the profiles of AA' and BB'. (b) Observed (blue line) and synthetic (red line) receiver functions at a station (magenta triangle in panels a, d, and e). (c) The radial (blue line) and vertical (red line) components of the adjoint source windowed around the Pms phase. The narrow time window selected in this specific example is to demonstrate the sensitivity of the Pms wave to *Vp*, *Vs*, and density. Cross sections along the profiles AA' and BB' show the event kernels with respect to *Vp* (d, e), *Vs* (f, g), and density (h, i).

This expanded sensitivity range is achieved by the finite-frequency kernel, which surpasses the sensitivity range provided by the ray-based kernel (Millet et al., 2019). Additionally, the *Vs* and density kernels indicate the sensitivity of other multiple phases, such as PpPs. Thus, we conclude that the *Vs* kernel contains more scattered phases than *Vp* and density kernels, and thus RFAT has better resolving ability in *Vs* than in *Vp* and density.

3.3. Numerical Tests

The effectiveness of RFAT in recovering *Vp*, *Vs*, and density models was assessed through a checkerboard test using the same virtual events and stations as in the real data inversion (see Text S2 in Supporting Information S1). With the Moho intentionally placed at ~35 km depth as the boundary between the crust and mantle, the test shows that the perturbations in *Vs* within the crust and uppermost mantle can be accurately resolved (Figures 3c and 3g). The *Vs* model exhibits higher resolution compared to *Vp* and density models. This is because both single and multiple scattered phases in the PRFs are sensitive to *Vs*. *Vp* anomalies are only well resolved in the crust, and smearing artifacts are visible along the incidence direction in the uppermost mantle (Figures 3b and 3f). Density anomalies are well resolved in the upper-mid crust (Figures 3d and 3h), but resolution is poor in the uppermost mantle. This limitation arises due to the fact that multiple scattered phases have higher sensitivities to density compared to single scattered phases (Figures 2h and 2i) (Julià, 2007). However, the short time window used in measuring the misfit function does not include enough multiply scattered phases generated in the uppermost mantle. To examine the impact of real noise in the PRFs on resolution, we further conducted resolution testing using discrete spikes and observed PRFs (Text S3 and Figure S9 in Supporting Information S1). Overall, the anomalies along the profile AA' with a dense array are better recovered than off-line areas with a larger station spacing, and the perturbations in *Vs* are more accurately resolved in the crust and uppermost mantle than those in *Vp* and density.

4. Tomographic Results and Discussion

4.1. Tomographic Results

The final models for *Vp*, *Vs*, and density (**M**12) were obtained using RFAT with 12 iterations. The reliability of **M**12 is demonstrated by the robustness test (Text S4, Figure S11 and S12 in Supporting Information S1). We will

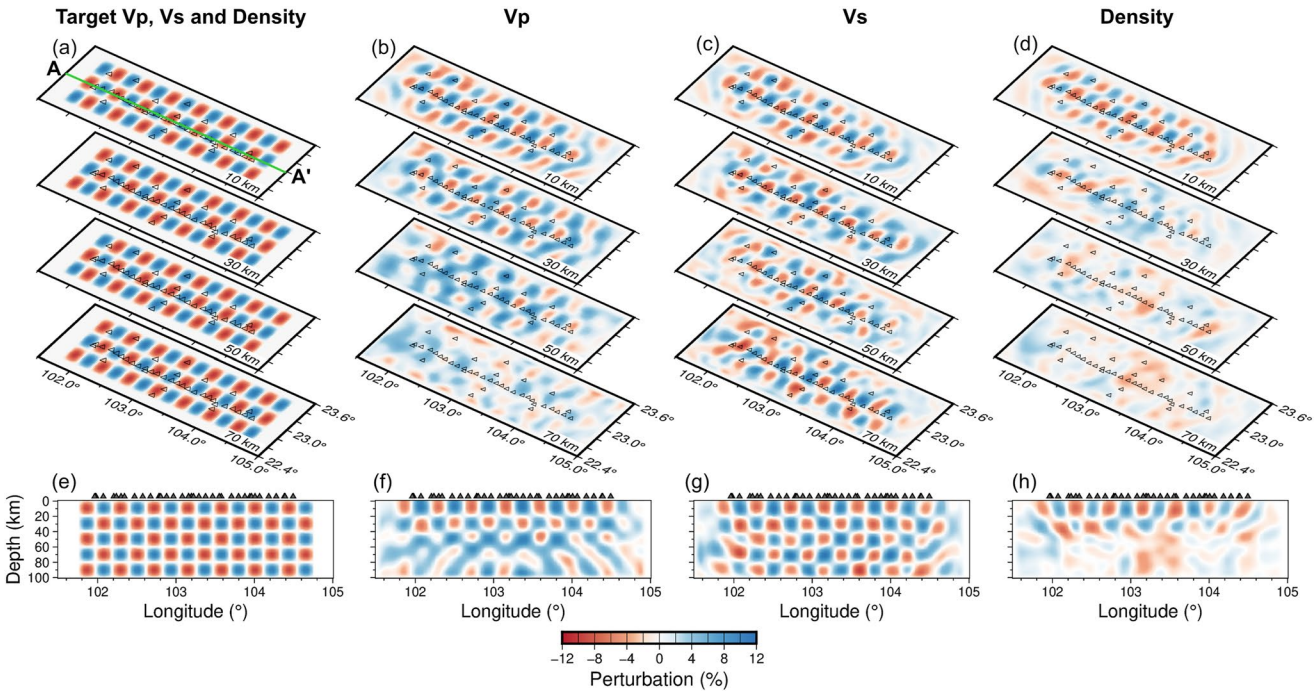

Figure 3. The 3-D checkerboard test for the receiver function adjoint tomography. The perturbations in *Vp*, *Vs* and density of the target model relative to the initial model are shown in horizontal slices (a) at depths of 10, 30, 50, and 70 km, and in the vertical section (e) along the AA' profile (green line in panel (a)). Panels (b)–(d) show the recovered perturbations of *Vp*, *Vs* and density, respectively. Panels (f)–(h) show the inverted perturbations of *Vp*, *Vs*, and density in the vertical section, respectively.

focus on the *Vs* model and its features along profile AA' because of their higher resolution (Figures 4b and 4c). The *Vp* and density models are displayed in Figure S7 in Supporting Information S1.

M12 reveals significant low-velocity zones (LVZs) in both the uppermost mantle and lower crust of the Indochina block, as well as in the lower crust of the ARSZ. Notably, the LVZ extends eastward from the lower crust down to the uppermost mantle under the boundary fault RRF (green arrow in Figure 4b). A resolution test of the "point spread function" (Fichtner & Trampert, 2011) is conducted to validate the robustness of this LVZ (Text S3 and Figure S10 in Supporting Information S1). The anomalies situated at the LVZ can be accurately resolved by real PRFs without visible smearing artifacts. The Moho discontinuity, determined by the maximum gradient of *Vs* between 25 and 45 km, is located at an average depth of ∼35 km (Figures 4b and 4c). In comparison to the flat Moho obtained by the CCP stacking (M. Xu et al., 2022), the Moho extracted from **M**12 exhibits lateral undulations beneath the ARSZ. Specifically, the Moho in **M**12 dips eastward under the RRF.

4.2. Comparison With the 1-D Joint Inversion of PRFs and SWDs

We compared the S-wave velocity model generated by RFAT (**M**12) with that generated by the 1-D joint inversion ($\mathbf{M}_{\text{joint}}$. See Text S5 in Supporting Information S1 for the details) (Figures 4c and 4d). Generally, both **M**12 and $\mathbf{M}_{\text{joint}}$ demonstrate similar lateral variations of S-wave velocity, highlighting the LVZs in the lower crust of the Indochina block and ARSZ, as well as high velocities in the uppermost mantle of the ARSZ and Yangtze craton. However, significant differences emerge near the RRF. **M**12 reveals not only LVZs that extend eastward from the lower crust down to the uppermost mantle beneath the RRF but also an eastward-dipping Moho, which are absent in $\mathbf{M}_{\text{joint}}$.

To evaluate the reliability and effectiveness of RFAT, we compare the observed PRFs with the synthetic PRFs computed in both **M**12 and $\mathbf{M}_{\text{joint}}$. Figures 4e–4g show the observed and synthetic PRFs at station X1.53188, which is located above the eastward-dipping Moho. The intracrustal and Pms phases of the observed PRFs show different characteristics in back-azimuth. The RFAT-generated PRFs match better with the observed PRFs in almost all back-azimuths compared to PRFs generated by the $\mathbf{M}_{\text{joint}}$ (Figure 4e). When windowed from 1 to 8 s,

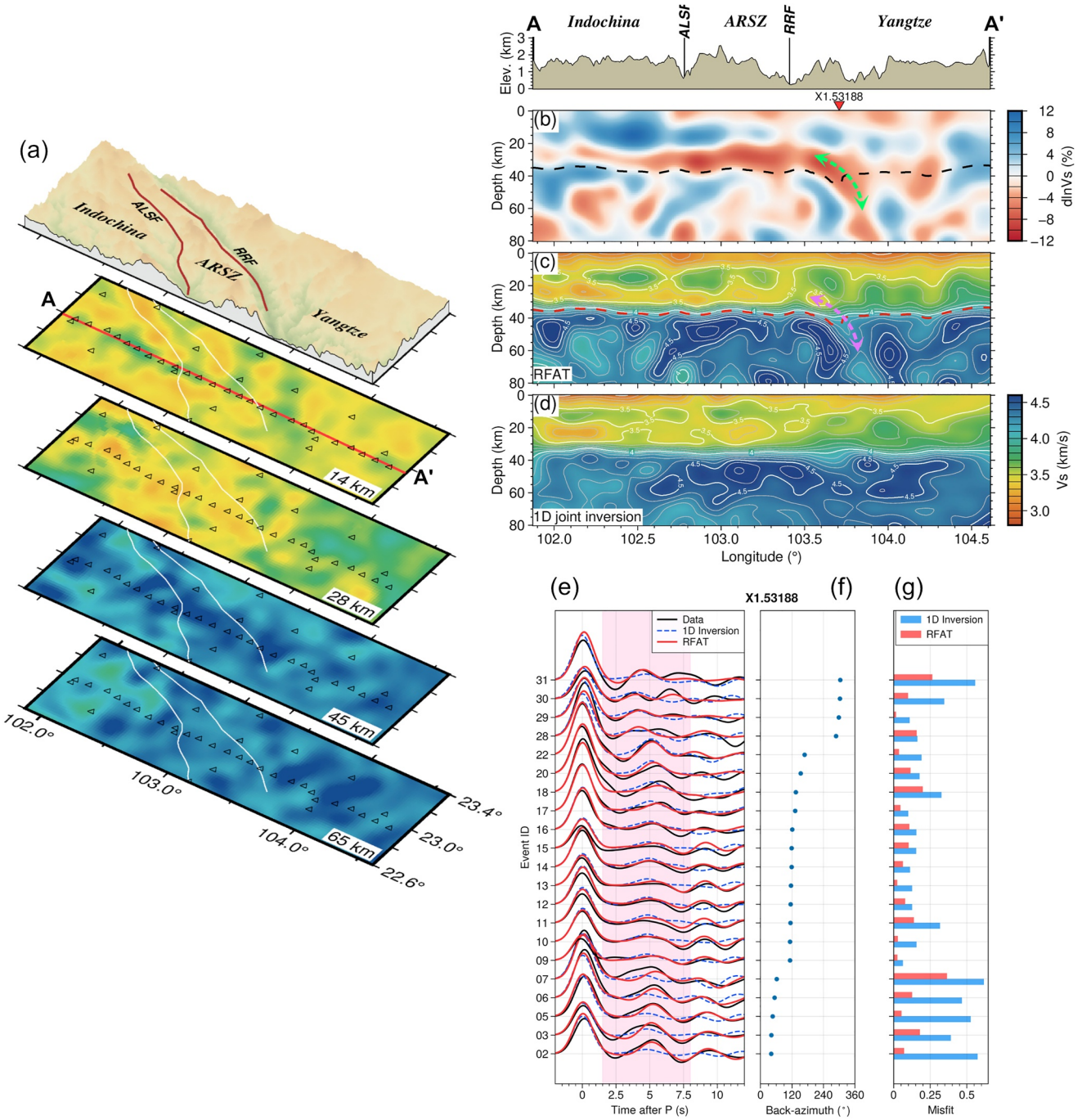

Figure 4. (a) Map views of the Vs model at depths of 14, 28, 45, and 65 km. (b) Cross-section of the Vs anomalies relative to **M**00 along profile AA' (red line in panel (a)). Panels (c) and (d) demonstrate cross sections of the *Vs* model along AA' revealed by the receiver function adjoint tomography (RFAT) and the 1-D joint inversion of P-wave receiver functions (PRFs) and surface wave dispersions, respectively. The respective green and magenta arrows in panels (b) and (c) denote the extending direction of the low-velocity zone. The dashed lines in panels (b) and (c) denote the Moho. (e) The observed PRFs (black curves), the synthetic PRFs computed in the model generated by RFAT (red curves), and the synthetic PRFs computed in the final model generated by the 1-D joint inversion (blue dashed curves) at station X1.53188. The pink area indicates the time window for measuring misfits around the Ps phase between the observed and synthetic PRFs. (f) The corresponding back-azimuth of each event. (g) The measured misfit for each event.

the misfits involving intracrustal and Pms phases between the observed PRFs and RFAT-generated PRFs are smaller, and less fluctuating compared to those derived from the $\mathbf{M}_{\text{joint}}$ (Figure 4g). However, a small number of RFAT-generated RFs do not fit the observed RFs well, possibly due to interference of noise and complex

scattered phases. RFAT's higher PRF fit indicates reliable eastward-dipping Moho and LVZs beneath the RRF. The tomographic results also demonstrate that RFAT has improved resolution and accuracy in resolving lateral heterogeneities compared to the 1-D joint inversion.

4.3. Geodynamic Implications

The ARSZ has a significant history of magmatic activity dating back to the Cenozoic (J. Liu et al., 2020; J. Zhang et al., 2017). Isotopic geochemical studies suggest that this magmatic activity involves both crustal and mantle components (J. Liu et al., 2020; L.-L. Xu et al., 2019), indicating the asthenospheric upwelling beneath the Indochina block. This interpretation is further supported by geophysical observations, such as the LVZs in the uppermost mantle found by our study and previous results (Han et al., 2022; Nábělek et al., 2009; Z. Zhang et al., 2020b), a thin lithosphere (Pasyanos et al., 2014; M. Xu et al., 2022), and low-resistivity anomalies (Yu et al., 2020). The RRF was reactivated in the Cenozoic (Tapponnier et al., 1990), making it a potential channel for the asthenospheric upwelling to the crust (Hou et al., 2022). The LVZs and eastward-dipping Moho under the RRF, revealed by our study, provide direct evidence for the detailed transport of the hot mantle materials. Under asthenosphere upwelling conditions, the lower crustal LVZs observed in our S-wave velocity model imply partial melting, as evidenced by the existence of crustal components in the metamorphic rocks (J. Liu et al., 2020), high crustal Poisson's ratio (L. Zhang et al., 2020a), and high heat flow (Jiang et al., 2019). Thus, we believe that the RRF is a channel for asthenospheric upwelling, and the heat inflow along this channel leads to partial melting in the lower crust, forming a significant amount of magmatic activities.

5. Conclusions

We have developed an inversion framework for adjoint tomography of PRFs (RFAT) that utilizes both single and multiple scattering phases to invert for *Vp*, *Vs*, and density models. RFAT removes the source signature from teleseismic waveforms, enabling reliable use of high-frequency PRFs (~1 Hz) for adjoint tomography. As a result, the RFAT provides higher-resolution images of crustal and uppermost mantle structures with lateral heterogeneities than traditional 1-D joint inversion.

We employed the RFAT to image the crustal and uppermost mantle structure across the ARSZ in southeastern Tibet. The resulting 3-D S-wave velocity model demonstrates LVZs extending eastward from the lower crust to the uppermost mantle and an eastward-dipping Moho beneath the RRF. These findings provide direct evidence that the RRF, as a channel, controls Cenozoic upwelling from the asthenosphere to the crust. The results demonstrate the effectiveness of RFAT in accurately imaging subsurface structures and providing valuable insights into geological structures and processes.

Acknowledgments
We thank Prof. Germán Prieto (editor), Prof. Vadim Levin and another two anonymous reviewers for their valuable comments, which have greatly improved the paper. This study was supported by the Ministry of Education, Singapore, under its MOE AcRF Tier 2_February 2022 Grant Call (MOE-T2EP20122-0008). MX, KW and PT were partially supported by the National Research Foundation Singapore and Singapore Ministry of Education under the Research Centers of Excellence Initiative (04MNS001913A620). This study was also funded by the National Key R&D Program of China (2016YFC0600302). The receiver functions were measured using the open-source software Seispy (M. Xu & He, 2022). The joint inversion of receiver functions and surface wave dispersions was performed using the CPS330 (Herrmann, 2013). Figures were made by GMT 6 (Wessel et al., 2019) and Matplotlib (Hunter, 2007).

Data Availability Statement

The P-wave receiver functions for this study can be downloaded at https://doi.org/10.21979/N9/MBWEP5. The initial model for this study can be downloaded from the supplementary file of Z. Zhang et al. (2020b). The open-source software SPECFEM3D (Komatitsch & Vilotte, 1998) is used for forward and adjoint simulations of wavefields (https://geodynamics.org/resources/specfem3dcartesian). The full-waveform adjoint tomography (FWAT) package can be downloaded at K. Wang (2021) (https://doi.org/10.5281/zenodo.4747811).

References

Ammon, C. J., Randall, G. E., & Zandt, G. (1990). On the nonuniqueness of receiver function inversions. *Journal of Geophysical Research*, *95*(B10), 15303–15318. https://doi.org/10.1029/JB095iB10p15303

Beller, S., Monteiller, V., Operto, S., Nolet, G., Paul, A., & Zhao, L. (2018). Lithospheric architecture of the South-Western Alps revealed by multiparameter teleseismic full-waveform inversion. *Geophysical Journal International*, *212*(2), 1369–1388. https://doi.org/10.1093/gji/ggx216

Bodin, T., Sambridge, M., Tkalčić, H., Arroucau, P., Gallagher, K., & Rawlinson, N. (2012). Transdimensional inversion of receiver functions and surface wave dispersion. *Journal of Geophysical Research*, *117*(B2), B02301. https://doi.org/10.1029/2011JB008560

de Jong, J. H. E., Paulssen, H., van Leeuwen, T., & Trampert, J. (2022). Sensitivity kernels for receiver function misfits in a full waveform inversion workflow. *Geophysical Journal International*, *230*(2), 1065–1079. https://doi.org/10.1093/gji/ggac098

Dueker, K. G., & Sheehan, A. F. (1997). Mantle discontinuity structure from midpoint stacks of converted P to S waves across the yellowstone hotspot track. *Journal of Geophysical Research*, *102*(B4), 8313–8327. https://doi.org/10.1029/96JB03857

Fichtner, A., Bunge, H., & Igel, H. (2006). The adjoint method in seismology: I. Theory. *Physics of the Earth and Planetary Interiors*, *157*(1–2), 86–104. https://doi.org/10.1016/j.pepi.2006.03.016

Fichtner, A., & Trampert, J. (2011). Hessian kernels of seismic data functionals based upon adjoint techniques: Hessian kernels. *Geophysical Journal International*, *185*(2), 775–798. https://doi.org/10.1111/j.1365-246X.2011.04966.x

Han, C., Huang, Z., Hao, S., Wang, L., Xu, M., & Hammond, J. O. S. (2022). Restricted lithospheric extrusion in the SE Tibetan Plateau: Evidence from anisotropic Rayleigh-wave tomography. *Earth and Planetary Science Letters*, *598*, 117837. https://doi.org/10.1016/j.epsl.2022.117837

Hansen, S. M., & Schmandt, B. (2017). *P* and *S* Wave receiver function imaging of subduction with scattering kernels: Receiver function kernel imaging. *Geochemistry, Geophysics, Geosystems*, *18*(12), 4487–4502. https://doi.org/10.1002/2017GC007120

Herrmann, R. B. (2013). Computer programs in seismology: An evolving tool for instruction and research. *Seismological Research Letters*, *84*(6), 1081–1088. https://doi.org/10.1785/0220110096

Hou, Z., Wang, Q., Zhang, H., Xu, B., Yu, N., Wang, R., et al. (2022). Lithosphere architecture characterized by crust-mantle decoupling controls the formation of orogenic gold deposits. *National Science Review*, *10*(3), nwac257. https://doi.org/10.1093/nsr/nwac257

Hunter, J. D. (2007). Matplotlib: A 2D graphics environment. *Computing in Science & Engineering*, *9*(3), 90–95. https://doi.org/10.1109/MCSE.2007.55

Jiang, G., Hu, S., Shi, Y., Zhang, C., Wang, Z., & Hu, D. (2019). Terrestrial heat flow of continental China: Updated dataset and tectonic implications. *Tectonophysics*, *753*, 36–48. https://doi.org/10.1016/j.tecto.2019.01.006

Julià, J. (2007). Constraining velocity and density contrasts across the crust-mantle boundary with receiver function amplitudes. *Geophysical Journal International*, *171*(1), 286–301. https://doi.org/10.1111/j.1365-2966.2007.03502.x

Julià, J., Ammon, C. J., Herrmann, R. B., & Correig, A. M. (2000). Joint inversion of receiver function and surface wave dispersion observations. *Geophysical Journal International*, *143*(1), 99–112. https://doi.org/10.1046/j.1365-246x.2000.00217.x

Komatitsch, D., & Vilotte, J.-P. (1998). The spectral element method: An efficient tool to simulate the seismic response of 2D and 3D geological structures. *Bulletin of the Seismological Society of America*, *88*(2), 368–392. https://doi.org/10.1785/BSSA0880020368

Langston, C. A. (1979). Structure under Mount Rainier, Washington, inferred from teleseismic body waves. *Journal of Geophysical Research*, *84*(B9), 4749–4762. https://doi.org/10.1029/JB084iB09p04749

Lekic, V., French, S. W., & Fischer, K. M. (2011). Lithospheric thinning beneath rifted regions of Southern California. *Science*, *334*(6057), 783–787. https://doi.org/10.1126/science.1208898

Ligorría, J. P., & Ammon, C. J. (1999). Iterative deconvolution and receiver-function estimation. *Bulletin of the Seismological Society of America*, *89*(5), 1395–1400. https://doi.org/10.1785/BSSA0890051395

Liu, D. C., & Nocedal, J. (1989). On the limited memory BFGS method for large scale optimization. *Mathematical Programming*, *45*(1), 503–528. https://doi.org/10.1007/BF01589116

Liu, J., Chen, X., Tang, Y., Song, Z., & Wang, W. (2020). The Ailao Shan–Red River shear zone revisited: Timing and tectonic implications. *GSA Bulletin*, *132*(5–6), 1165–1182. https://doi.org/10.1130/B35220.1

Liu, Q., & Tromp, J. (2006). Finite-frequency kernels based on adjoint methods. *Bulletin of the Seismological Society of America*, *96*(6), 2383–2397. https://doi.org/10.1785/0120060041

Liu, Q., & Tromp, J. (2008). Finite-frequency sensitivity kernels for global seismic wave propagation based upon adjoint methods. *Geophysical Journal International*, *174*(1), 265–286. https://doi.org/10.1111/j.1365-246X.2008.03798.x

Millet, F., Bodin, T., & Rondenay, S. (2019). Multimode 3-D Kirchhoff migration of receiver functions at continental scale. *Journal of Geophysical Research: Solid Earth*, *124*(8), 8953–8980. https://doi.org/10.1029/2018JB017288

Monteiller, V., Chevrot, S., Komatitsch, D., & Wang, Y. (2015). Three-dimensional full waveform inversion of short-period teleseismic wavefields based upon the SEM–DSM hybrid method. *Geophysical Journal International*, *202*(2), 811–827. https://doi.org/10.1093/gji/ggv189

Murtagh, F., & Legendre, P. (2014). Ward's hierarchical agglomerative clustering method: Which algorithms implement ward's criterion? *Journal of Classification*, *31*(3), 274–295. https://doi.org/10.1007/s00357-014-9161-z

Nábělek, J., Hetényi, G., Vergne, J., Sapkota, S., Kafle, B., Jiang, M., et al. (2009). Underplating in the Himalaya-Tibet collision zone revealed by the Hi-CLIMB experiment. *Science*, *325*(5946), 1371–1374. https://doi.org/10.1126/science.1167719

Pasyanos, M. E., Masters, T. G., Laske, G., & Ma, Z. (2014). LITHO1.0: An updated crust and lithospheric model of the Earth. *Journal of Geophysical Research: Solid Earth*, *119*(3), 2153–2173. https://doi.org/10.1002/2013JB010626

Ruan, Y., Lei, W., Modrak, R., Örsvuran, R., Bozdağ, E., & Tromp, J. (2019). Balancing unevenly distributed data in seismic tomography: A global adjoint tomography example. *Geophysical Journal International*, *219*(2), 1225–1236. https://doi.org/10.1093/gji/ggz356

Stacey, R. (1988). Improved transparent boundary formulations for the elastic-wave equation. *Bulletin of the Seismological Society of America*, *78*(6), 2089–2097. https://doi.org/10.1785/BSSA0780062089

Tapponnier, P., Lacassin, R., Leloup, P. H., Schärer, U., Dalai, Z., Haiwei, W., et al. (1990). The Ailao Shan/Red River metamorphic belt: Tertiary left-lateral shear between Indochina and South China. *Nature*, *343*(6257), 431–437. https://doi.org/10.1038/343431a0

Tong, P., Chen, C., Komatitsch, D., Basini, P., & Liu, Q. (2014a). High-resolution seismic array imaging based on an SEM-FK hybrid method. *Geophysical Journal International*, *197*(1), 369–395. https://doi.org/10.1093/gji/ggt508

Tong, P., Komatitsch, D., Tseng, T.-L., Hung, S.-H., Chen, C.-W., Basini, P., & Liu, Q. (2014b). A 3-D spectral-element and frequency-wave number hybrid method for high-resolution seismic array imaging. *Geophysical Research Letters*, *41*(20), 7025–7034. https://doi.org/10.1002/2014GL061644

Tromp, J., Tape, C., & Liu, Q. (2005). Seismic tomography, adjoint methods, time reversal and banana-doughnut kernels. *Geophysical Journal International*, *160*(1), 195–216. https://doi.org/10.1111/j.1365-246X.2004.02453.x

Wang, K. (2021). Full-waveform adjoint tomography package (v1.0) [Computer software]. Zenodo. https://doi.org/10.5281/zenodo.4747811

Wang, K., Wang, Y., Song, X., Tong, P., Liu, Q., & Yang, Y. (2021a). Full-waveform inversion of high-frequency teleseismic body waves based on multiple plane-wave incidence: Methods and practical applications. *Bulletin of the Seismological Society of America*, *112*(1), 118–132. https://doi.org/10.1785/0120210094

Wang, K., Yang, Y., Jiang, C., Wang, Y., Tong, P., Liu, T., & Liu, Q. (2021b). Adjoint tomography of ambient noise data and teleseismic P waves: Methodology and applications to Central California. *Journal of Geophysical Research: Solid Earth*, *126*(6). https://doi.org/10.1029/2021JB021648

Wang, Y., Chevrot, S., Monteiller, V., Komatitsch, D., Mouthereau, F., Manatschal, G., et al. (2016). The deep roots of the western Pyrenees revealed by full waveform inversion of teleseismic P waves. *Geology*, *44*(6), 475–478. https://doi.org/10.1130/G37812.1

Wessel, P., Luis, J. F., Uieda, L., Scharroo, R., Wobbe, F., Smith, W. H. F., & Tian, D. (2019). The generic mapping tools version 6. *Geochemistry, Geophysics, Geosystems*, *20*(11), 5556–5564. https://doi.org/10.1029/2019GC008515

Xu, L.-L., Bi, X.-W., Hu, R.-Z., Tang, Y.-Y., Wang, X.-S., Huang, M.-L., et al. (2019). Contrasting whole-rock and mineral compositions of ore-bearing (Tongchang) and ore-barren (Shilicun) granitic plutons in SW China: Implications for petrogenesis and ore genesis. *Lithos*, *336–337*, 54–66. https://doi.org/10.1016/j.lithos.2019.03.031

Xu, M., & He, J. (2022). Seispy: Python module for batch calculation and postprocessing of receiver functions. *Seismological Research Letters*, *94*(2A), 935–943. https://doi.org/10.1785/0220220288

Xu, M., Huang, Z., Wang, L., Xu, M., Zhang, Y., Mi, N., et al. (2020). Sharp lateral Moho variations across the SE Tibetan margin and their implications for plateau growth. *Journal of Geophysical Research: Solid Earth*, *125*(5). https://doi.org/10.1029/2019JB018117

Xu, M., Yu, D., Huang, Z., Tong, P., Hao, S., Ruan, Y., & Han, C. (2022). Crustal and uppermost mantle heterogeneities across the Ailaoshan Red River shear zone, SE Tibet: Implications for cenozoic magmatic activity. *Journal of Geophysical Research: Solid Earth*, *127*(6). https://doi.org/10.1029/2021JB023656

Yu, N., Unsworth, M., Wang, X., Li, D., Wang, E., Li, R., et al. (2020). New insights into crustal and mantle flow beneath the red river fault zone and adjacent areas on the southern margin of the Tibetan plateau revealed by a 3-D magnetotelluric study. *Journal of Geophysical Research: Solid Earth*, *125*(10). https://doi.org/10.1029/2020JB019396

Zhang, J., Wang, H., Li, S., & Li, T. (2017). Paleogene magmatism and gold metallogeny of the Jinping terrane in the Ailaoshan ore belt, Sanjiang Tethyan Orogen (SW China): Geology, deposit type and tectonic setting. *Ore Geology Reviews*, *91*, 620–637. https://doi.org/10.1016/j.oregeorev.2017.08.032

Zhang, L., Bai, Z., Xu, T., Wu, Z., Huang, M., Yu, G., et al. (2020a). Cenozoic magmatic activity and oblique uplifting of the Ailao Mountain: Evidence from a short-period dense seismic array. *Science China Earth Sciences*, *63*(9), 1294–1308. https://doi.org/10.1007/s11430-019-9616-y

Zhang, Z., Yao, H., & Yang, Y. (2020b). Shear wave velocity structure of the crust and upper mantle in Southeastern Tibet and its geodynamic implications. *Science China Earth Sciences*, *63*(9), 1278–1293. https://doi.org/10.1007/s11430-020-9625-3

Zhu, H., Bozdağ, E., & Tromp, J. (2015). Seismic structure of the European upper mantle based on adjoint tomography. *Geophysical Journal International*, *201*(1), 18–52. https://doi.org/10.1093/gji/ggu492

Zhu, L., & Kanamori, H. (2000). Moho depth variation in southern California from teleseismic receiver functions. *Journal of Geophysical Research*, *105*(B2), 2969–2980. https://doi.org/10.1029/1999jb900322

References From the Supporting Information

Brocher, T. M. (2005). Empirical relations between elastic wavespeeds and density in the Earth's crust. *Bulletin of the Seismological Society of America*, *95*(6), 2081–2092. https://doi.org/10.1785/0120050077

Modrak, R., & Tromp, J. (2016). Seismic waveform inversion best practices: Regional, global and exploration test cases. *Geophysical Journal International*, *206*(3), 1864–1889. https://doi.org/10.1093/gji/ggw202

Monteiller, V., Beller, S., Plazolles, B., & Chevrot, S. (2020). On the validity of the planar wave approximation to compute synthetic seismograms of teleseismic body waves in a 3-D regional model. *Geophysical Journal International*, *224*(3), 2060–2076. https://doi.org/10.1093/gji/ggaa570

Shen, W., Ritzwoller, M. H., Kang, D., Kim, Y. H., Lin, F. C., Ning, J., et al. (2016). A seismic reference model for the crust and uppermost mantle beneath China from surface wave dispersion. *Geophysical Journal International*, *206*(2), 954–979. https://doi.org/10.1093/gji/ggw175